

LASER PLASMA

PACS numbers: 52.50.Jm; 52.70.Kz
DOI: 10.1070/QE2011v041n01ABEH014460

Density jumps in the plasma of a nanosecond laser-induced spark and their dynamics

A.A. Malyutin, V.A. Podvyaznikov, V.K. Chevokin

Abstract. **Experimental investigation of the structure of a laser-induced spark emerging in the focusing of 50-ns radiation pulses is described. Two density jumps were discovered in the plasma of the laser-induced spark. One of them is localised in the vicinity of the focal plane of the lens, the other propagates from this plane in the laser propagation direction at a constant velocity of ~ 7.5 km s^{-1}.**

Keywords: *laser-induced spark, plasma, density jumps.*

1. Introduction

Laser-induced plasma production, which was first demonstrated by Maker et al. [1] in the air, today is realisable in the volume or on the surface of practically all gaseous, liquid, and solid substances. Available wavelength, duration, and power ranges of modern laser pulses offer endless possibilities for the investigations and applications of this plasma. In particular, laser-spark emission spectrometry (LSES) nowadays is used in material science, medicine, and ecology, as well as in archaeology, forensic science, and art history. The reliability, sensitivity, and accuracy of LSES, like of any other application of laser-produced plasma, depend to a large measure on the depth of insight into the physical processes occurring therein; the study of these processes involves, first of all, the study of morphology, i.e. of the plasma structure: its geometry, density, radiation, temperature, etc., and its temporal variation.

It is likely that the first description of a spark produced in the air by nanosecond laser pulses was given by Young et al. [2]: 'At the center of the spark is an extremely intense core in the form of a narrow cylinder aligned along the lens axis. Surrounding this core is a region of lesser intensity which is generally divided into lobes or striations... the sparks are essentially reproducible in all their observable detail... Surrounding this second region is a structureless cloud probably made up of excited atoms rather than ions and electrons.' Subsequent works using nanosecond pulses, including recent publications, have not added much new data to this description. It only became clear that the first of the spark regions singled out by the authors of Ref. [2] is associated with the laser radiation reflected at the plasma – unperturbed gas boundary [3 – 6], while the second is the plasma itself, which expands primarily towards the focusing lens. It is noteworthy that the authors of Ref. [2] also give a schematic representation of the spark, wherein the focal plane of the lens falls into the gap between its two lobes. This fact, which is rather an assumption than an experimental result of Ref. [2], has not been disproved, confirmed, or even mentioned in any of the papers known to us. This being so despite the fact that the spark structure, as a rule, does coincide with the structure described in Ref. [2], even though the intrinsic radiation of the spark plasma may be recorded several, tens, or many hundred nanoseconds after breakdown [7 – 13].

Also observed were spark structures more complex than that described in Ref. [2], especially so when use was made of long-focus lenses and laser radiation energies far exceeding the breakdown threshold intensities. When illuminated by laser light, these structures had the form of thin tracks and dots (bead-like structure) [3 – 6, 14 – 17]; when shadow and schlieren methods were employed [18 – 21], they appeared in the form of an extended object, which expanded towards the lens and was rather symmetric about its axis. It was noted that this object might have narrow gaps interpreted as collisions of plasma fronts and/or shock waves. The occurrence of gaps was attributed to the emergence of a breakdown and the energy liberation at different points along the lens axis.

The internal plasma structure of the laser-induced spark was also investigated by the methods of holographic interferometry [22]. It was found that the electron density in the laser-induced air breakdown may range up to $\sim 8 \times 10^{19}$ cm^{-3} at the plasma front facing the focusing lens. In hydrogen and helium, appreciable density gradients are sometimes not observed in the volume, but in some cases they emerge in the end of the spark farthest from the lens [20]. A similar effect was observed in Ref. [23].

Three possible causes of the emergence of a complex structure in the plasma of laser-induced laser sparks are mentioned in the literature [24]: the multimodal composition of laser radiation, aberrations of focal lenses, and the breakdown on aerosols and dust particles.

The role of the first of the foregoing causes was significant in the experiments that date back to the 1960s – 1970s, especially so when ruby lasers were involved. In recent research [7 – 13], advantage was primarily taken of commercial YAG : Nd crystal lasers, whose beam quality is quite high, as a rule. At least this applies to spatio-angular

A.A. Malyutin, V.A. Podvyaznikov, V.K. Chevokin A.M. Prokhorov General Physics Institute, Russian Academy of Sciences, ul. Vavilova, 38, 119991 Moscow, Russia; e-mail: amal@kapella.gpi.ru

Received 22 October 2010
Kvantovaya Elektronika **41** (1) 38 – 42 (2011)
Translated by E.N. Ragozin

beam parameters. True, the absence of longitudinal mode selection (particularly in the electrooptical Q-switching) makes the temporal pulse structure indefinite, which may escape detection by an oscilloscope and give rise to the corresponding spark structure (especially so when observations are performed at the same wavelength as the wavelength of the spark-forming radiation). When the temporal resolution is not better than 10^{-9} s, for a measured plasma-front velocity of $10^6 - 10^7$ cm s^{-1} the case in point may be the characteristic dimension not exceeding 10–100 μm [25].

As shown in Refs [21, 26, 27], lens aberrations do exert a strong effect on the spark structure. With rare exception [8–11], however, even in recent years this issue has not received proper attention and use has been made of plano-spherical lenses. Their use in investigations is supposedly admissible only late in the development of the laser-induced plasma – hundreds of microseconds after breakdown and shock separation from the plasma body. This is confirmed, in particular, by good agreement between experimental results [29] and the data of numerical simulations with a rather arbitrary assignment of the initial parameters of a laser-induced spark [28].

As determined experimentally [30], dust pollution of the air affects the structure of laser-induced sparks when use is made of long-focus lenses and the beam diameter-to-focal length ratio is small ($D/F \ll 0.1$). For short-focus lenses and particle sizes much smaller than the wavelength of laser radiation, observed is only a lowering of the breakdown threshold [24].

As a continuation of our investigations of nanosecond laser-induced sparks [25, 31], our work is an effort to study in greater detail the internal structure of the generated plasma.

2. Experiment

As before [25, 31], our experiments employed the radiation of a neodymium glass laser with a pulse duration $\tau = 50\pm$ 5 ns and an energy of up to 70 mJ. The spatial radiation intensity distribution corresponded to the TEM_{00} mode.

To obtain air breakdown, the radiation was focused by aspherical lenses with focal lengths $F = 8$ and 20 mm, use was also made of an ordinary plano-spherical lens with $F = 50$ mm. In experiments the laser beam diameter $2w$ at the input to the focusing lenses was invariably equal to ~ 4 mm.

The spark plasma structure was investigated by shadow and schlieren techniques. For this purpose we employed a probe pulse with a duration $\tau \approx 4$ ns generated by a YAG : Nd crystal laser. The technique of timing the probe pulse to the 50-ns long neodymium glass laser pulses was described in Ref. [32]. The probe pulse delay relative to the instant of breakdown was measured using a Tektronix TDS5104B oscilloscope. The dark background version of the schlieren technique was employed, i.e. the lowest spatial frequencies were blocked by a mask 50 μm in diameter in the focal plane of a $3.5^{\times}/0.1$ imaging microlens. Placed in the image plane was either an Elphel 313 CMOS camera or, in spatio-temporal measurements, the entrance slit of a streak camera (SC) with a microchannel amplifier and a Videoscan-415-USB CCD detector. When operating the SC, the radiation of the main laser was employed as the probe radiation.

Figure 1 depicts the spark images obtained by the schlieren technique for different energies of laser radiation and probe pulse delays relative to the instant of air breakdown ($F = 8$ mm). We note the presence of interference fringes, which characterise the optical density of the spark plasma, and the characteristic transverse structure (density jump) in the vicinity of the focal plane of the focusing lens. The absence of interference fringes at the anterior plasma front propagating upstream of the laser beam is indication that the probe pulse is insufficiently short. Structures similar to those shown in Fig. 1 were also observed when use was made of the lenses with focal lengths $F = 20$ and 50 mm, both with the shadow (Fig. 2) and schlieren (Fig. 3) recording techniques. The bright track on the axis of spark images (Figs 1–3) is due to the laser radiation reflected at the anterior plasma front. The track structure, which was discussed in detail earlier [25, 31], was used to determine the position of the laser beam waist.

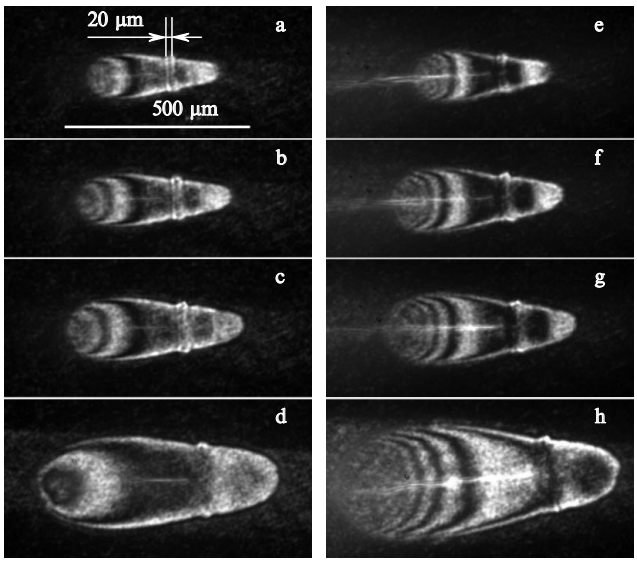

Figure 1. Spark images in the air obtained by the schlieren technique for laser radiation energies $E = 10$ (a–d) and 22 mJ (e–h), for probe pulse delays d$t = 7$ (a, e), 9.5 (b, f), 12.5 (c, g) and 24 ns (d, h) relative to the instant of air breakdown, $F = 8$ mm.

In the pursuance of spatio-temporal measurements, the image of the axial spark region was brought into coincidence with the SC entrance slit. Similar experiments were also conducted in our earlier work [31]. In particular, when measuring the velocity of plasma front propagation away from the focusing lens it was found that 35–40 ns after air breakdown, i.e. far behind the peak of the laser pulse, we observed a sharp rise in reflected radiation intensity (Fig. 4a). Judging by the general character of the signal one might draw a conclusion that this reflecting (or scattering) portion of the plasma front possesses a nearly constant velocity. However, the noisy image structure did not allow stating this with assurance. The time scans of the axial part of spark plasma images obtained by the schlieren and shadow techniques, which are given in Figs 4b, 4c and Fig. 4d, respectively (the beam propagation direction: from bottom to top), enabled us to trace in more detail the variations of the density and absorption at the anterior and rear fronts of the expanding spark plasma. Figure 4e

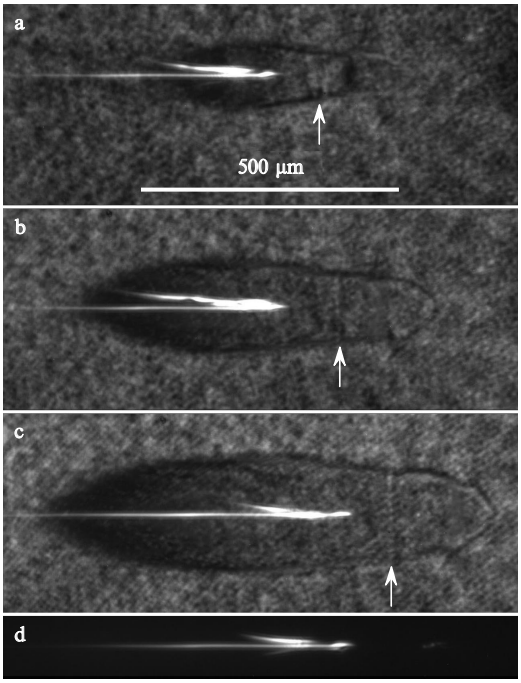

Figure 2. Images of spark in the air obtained by the shadow technique for probe pulse delays $dt = 4$ (a), 8 (b), and 12 ns (c) relative to the instant of air breakdown, as well as the time-integrated photograph of the spark at the wavelength of laser radiation (d). The energy of radiation $E \approx 14$ mJ, $F = 20$ mm. The position of the density jump in the focal plane of the lens is indicated with an arrow.

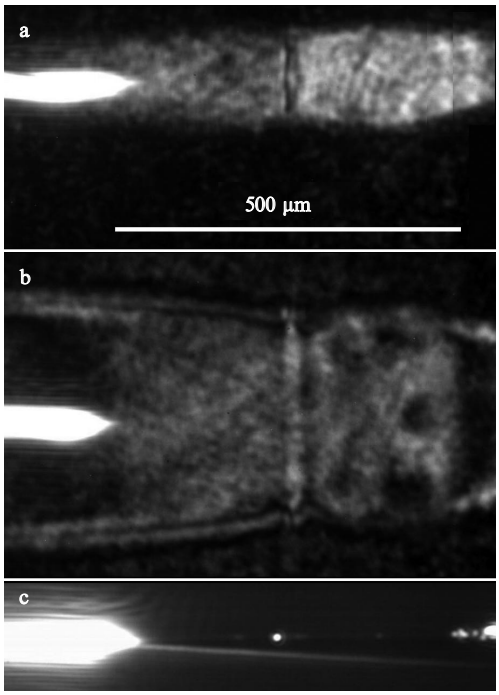

Figure 3. Fragments of the images of spark plasmas in the air obtained by the schlieren technique for probe pulse delays $dt = 4$ (a) and 14 ns (b), as well as integral photograph of the spark at the wavelength of laser radiation (c). The energy of radiation $E \approx 50$ mJ, $F = 50$ mm.

demonstrates the plasma dynamics with enhanced spatial and temporal resolution in the vicinity of the beam waist – the region of the emergence of air breakdown.

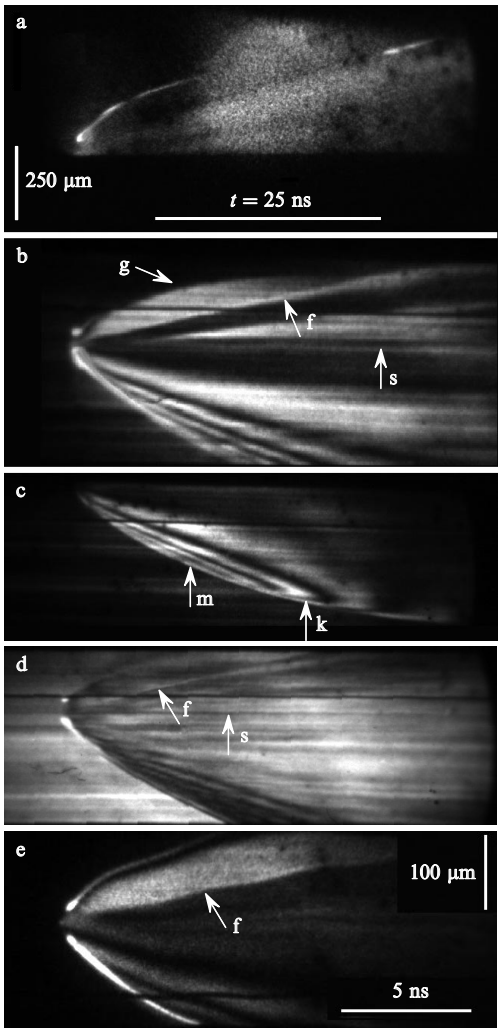

Figure 4. Spatio-temporal scans of the images of laser-induced spark plasma recorded in the scattered laser radiation (a), by the schlieren technique (b, c, e) (c – only the front propagating towards the focusing lens, e – image with enhanced spatial and temporal resolution) and by the shadow technique (d). See the text for the notation.

3. Discussion of experimental results

Because interpretation of the plasma images obtained by the schlieren technique is not as unambiguous as that in interferometric measurements, we begin our discussion of experimental data with consideration of the data of numerical simulations of the optical setup in use. In these simulations the refractive index of the spark plasma was defined by some function $dn(z)$ with a peak at the front facing the focusing lens [curve (*1*) in Fig. 5a]. The boundary of the plasma, which was assumed to be axially symmetric, was prescribed by the generatrix $R(z)$ [curve (*2*) in Fig. 5a]. The dimensions of the plasma body were taken approximately equal to the corresponding observed ones. Proceeding from these values and taking into account the delay introduced into the phase of the probe radiation, which propagates orthogonally to the axis of the plasma body, we calculated the phase screen

$$\Phi(x, z) = \frac{2dn}{\lambda}\sqrt{R^2(z) - x^2}, \quad x(z) \leqslant R(z)$$

and selected the maximum value of the function $dn(z)$ corresponding to the greatest on-axis phase incursion $\Phi(x=0,z) \approx 7\lambda$ [curve (*3*) in Fig. 5c]. Next, using the Fresnel code, numerical simulations were made of the passage of the probe beam through the screen $\Phi(x,z)$ in the optical configuration of the dark background version of the schlieren technique. The image at the output of the optical configuration (Fig. 5b) resulting from simulations is in rather good agreement with the images observed experimentally. The intensity distribution on the axis of the image (Fig. 5b) is represented by curve (*4*) in Fig. 5c. A comparison of the curves (*3*) and (*4*) in Fig. 5c suggests that the intensity maxima in Fig. 5b correspond to a semi-integer and the minima to an integer number of wavelengths in the phase distribution $\Phi(x,z)$.

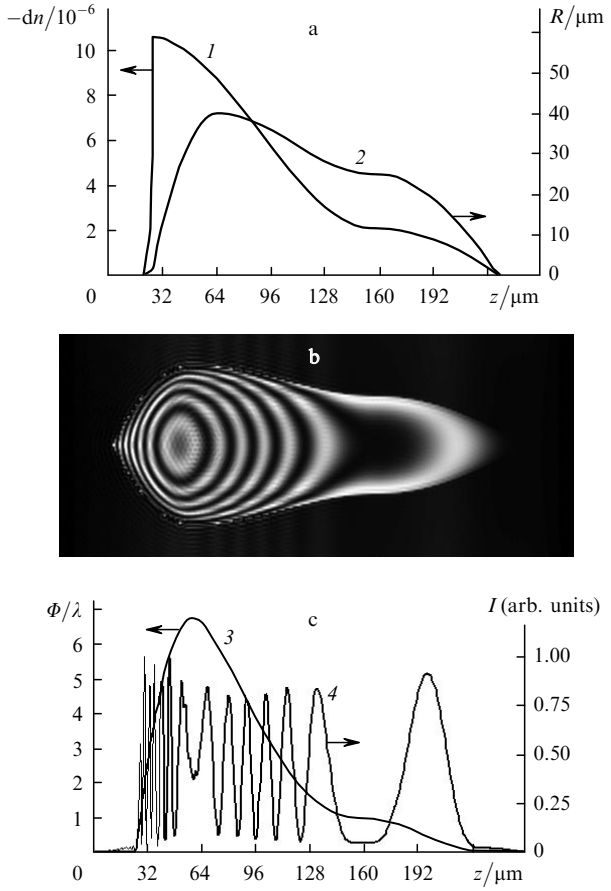

Figure 5. On computer simulations of the schlieren images of the spark plasma: plasma radius $R(z)$ and refractive index distribution $dn(z)$ adopted in the simulations (a), spark plasma image at the output of the optical setup (b), phase incursion and intensity distribution on the axis of spark plasma image (c).

If the assumptions made in the simulations are correct, to each of the maxima and minima observed in Fig. 1 it is possible to ascribe a definite value of the phase incursion. From schlieren measurements it is thereby possible to extract not only qualitative information, but also quantitative one. Figure 6 is an example of calculated distributions of the electron density N_e in the spark plasma $dt = 24$ ns after air breakdown by a laser pulse with an energy $E =$ 22 mJ. As the simulation suggest, in this instance for $\Phi_{max} = (5.5-6)\lambda$ the highest value $N_e = 1.2 \times 10^{20}$ cm^{-3}

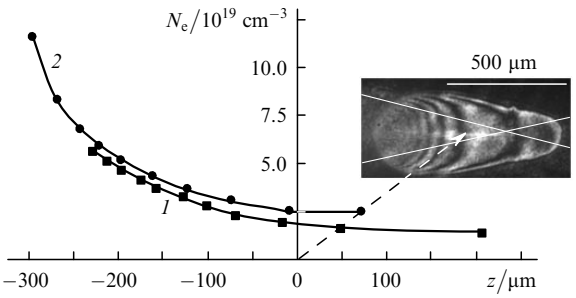

Figure 6. Electron density distribution $N_e(x,z)$ in the spark plasma on the axis ($x = 0$) (*1*) and for $x = 120$ μm (*2*). In the schlieren plasma image, the arrow indicates the point corresponding to $x = z = 0$, and lines of equal intensity in the laser beam are drawn at a level of e^{-1} of the peak value.

is reached at a distance of ~ 120 μm from the beam axis in the vicinity of the anterior plasma front. A small increase (by ~ 20 %) in N_e in comparison with its on-axis value is also observed in the radial direction.

The dynamics of N_e at the anterior plasma front may be judged by the temporal scan of the schlieren plasma image (Fig. 4c). In particular, approximately 15 ns after breakdown (this corresponds to mark m in Fig. 4c) the number of interference fringes and hence the electron density behind the front attain its peak. The steepness dN_e/dz at the plasma front supposedly assumes its peak value. A part of the interference fringes vanishes ~ 10 ns later (mark k), and the maximum of N_e moves away from the plasma – unperturbed gas boundary.

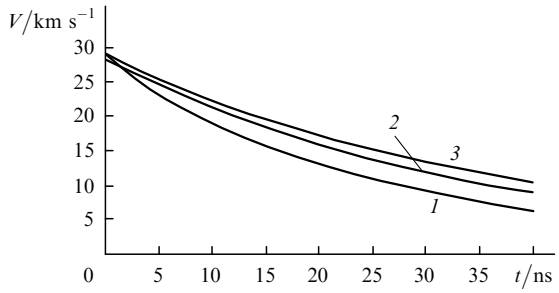

Figure 7. Time dependences of the propagation velocity of the anterior, travelling towards the focusing lens ($F = 8$ mm), front of air spark plasma for laser pulse energies of 10 (*1*), 30 (*2*), and 65 mJ (*3*). Each curve was obtained by averaging the measurements over 8 – 10 pulses.

According to measurements by the shadow technique (Fig. 2), the spark plasma exhibits rather high absorption in the domain adjacent to the front which travels towards the focusing lens. In this case, despite a significant lowering of the radiation energy density* with distance from the beam waist, the increase of the total energy E of the laser beam leads both to a growth of N_e behind the plasma front [$\Phi_{max} = (1.5-2.5)\lambda$ in the left column in Fig. 1 and $(5.5-6)\lambda$ in the right one] and to a rise in plasma expansion velocity (Fig. 7). To within experimental error, this increase in energy does not tell on the velocity of plasma motion immediately after breakdown ($t = 0$).

*For $F = 8$ mm, the beam radius in the beam waist is approximately 20 times less than at 100 μm from it.

The shadow and schlieren spark plasma images and their time scans show the existence of rather strong nonuniformities of N_e in the plasma volume. First and foremost, the case in point is the density jump which is stationary in position and located in (in the immediate vicinity of) the focal plane of the focusing lens (Figs 1–3). It is also seen, though with a lower contrast, in the scans of the spark plasma images (mark s in Figs 4b and 4d).

One can also see in Fig. 4d, which was obtained in the scanning of the shadow plasma image, that the spatial structures of the probe radiation prior to and after breakdown are different. However, this may be due not only to local variations of plasma absorption, but also to bulk changes of N_e. The latter possibility is attested by the visualisation of the interference fringes similar to those observed in the recording by the schlieren technique. Unlike the dark background schlieren technique, when the lowest spatial frequencies are rejected, in the case of the shadow technique the function of mask is played by the microlens aperture, which limits the highest spatial frequencies.

A feature also worthy of mention is the existence of a density jump (mark f in Fig. 4b) in the spark plasma. This density jump travels in the direction of laser radiation propagation. It is also seen in the scans of shadow image (Fig. 4d). The constant velocity of its propagation ($7-8$ km s^{-1}) and the position relative to the rear (traveling away from the focusing lens) plasma front (mark g) are in complete agreement with the observations of laser radiation scattering (Fig. 4a). As Fig. 4b suggests, the rear plasma front (mark g) decelerates and the jump (mark f) catches up with it at some point in time, which is responsible for a sharp rise in reflectivity of the plasma – unperturbed gas boundary. In this case, the intensity of the corresponding interference fringe in Fig. 4b is hardly changed. One may therefore draw a conclusion that the electron density N_e in the density jump attains its peak value when it reaches the plasma boundary: the path length in the plasma, which gives rise to the phase incursion for the probe radiation, becomes shorter as the jump approaches the front. The phase incursion is supposedly $\Phi \leqslant 0.5\lambda$.

A closer look at the data shows that the density jump has its origin (mark f) at the point of air breakdown in the focal plane of the lens (Fig. 4e). Also seen in Fig. 4e is a similar jump with a significantly lower density travelling in the opposite direction to the laser beam.

4. Conclusions

Laser-induced spark has been traditionally described as a sequence of three processes, the breakdown of gas in the field of high-power focused laser beam – the primary plasma production in the focal region; plasma expansion in the course of the laser pulse, when the plasma is within the caustic of the laser beam and propagates primarily towards the focusing lens; free expansion and cooling of the plasma. As our experiments suggest, engaged immediately after gas breakdown is an additional mechanism of the interaction between high-power laser radiation and the plasma, which has previously been neglected in connection with laser-induced sparks. It is supposedly this mechanism that is responsible for the emergence of at least two density jumps in the vicinity of laser beam waist: the stationary one, whose position remains invariable with time, and the jump travelling at a constant velocity of $7-8$ km s^{-1} in the direction of laser beam propagation. It is not unlikely that the spark structure in the form of two radiating domains, which is observable even hundreds of nanoseconds after cessation of the laser pulse [7–13], is also a result of the processes occurring in the laser beam waist at the earliest stages of spark development.

References

1. Maker P.D., Terhune R.W., Savage C.M. *Proc. 3rd Int. Conf. on Quantum Electronics* (New York: Columbia, 1963) p. 1559.
2. Young M., Hercher M., Wu C.J.Y. *J. Appl. Phys.*, **37**, 4938 (1966).
3. Savchenko M.M., Stepanov V.K. *Pis'ma Zh. Eksp. Teor. Fiz.*, **10**, 458 (1968).
4. Tomlinson R.G. *IEEE J. Quantum Electron.*, **5**, **591** (1969).
5. Ahmad N., Gale B.C., Key M.H. *J. Phys. B*, **2**, 403 (1969).
6. Wang C.C., Davis L.I. *Phys. Rev. Lett.*, **26**, 822 (1971).
7. Chen Y.-L., Lewis J.W.L. *Opt. Express*, **9**, 360 (2001).
8. Harilal S.S., Harilal B. Report UCSD-LPLM-02-02 (2002).
9. Bindhu C.V., Harilal S.S., Tillack M.S., Najmabadi F., Gaeris A.C. *J. Appl. Phys.*, **94**, 7402 (2003).
10. Bindhu C.V., Harilal S.S., Tillack M.S., Najmabadi F., Gaeris A.C. *Appl. Spectrosc.*, **58**, 719 (2004).
11. Harilal S.S. *Appl. Opt.*, **43**, 3931 (2004).
12. Glumac N., Elliott G., Boguszko M. *AIAA J.*, **43**, 1984 (2005).
13. Kawahara N., Beduneau J.L., Nakayama T., Tomita E., Ikeda Y. *Appl. Phys. B*, **86**, 605 (2007).
14. Mandel'shtam S.L., Pashinin P.P., Prokhorov A.M., Raizer Yu.P., Sukhodrev N.K. *Zh. Eksp. Teor. Fiz.*, **49**, 127 (1965).
15. Korobkin V.V., Mandel'shtam S.L., Pashinin P.P., Prokhindeev A.V., Prokhorov A.M., Sukhodrev N.K., Shchelev M.Ya. *Zh. Eksp. Teor. Fiz.*, **53**, 116 (1968).
16. Korobkin V.V., Alcock A.J. *Phys. Rev. Lett.*, **21**, 1433 (1968).
17. Key M.H., Preston D.A., Donaldson T.P. *J. Phys. B*, **3**, L88 (1970).
18. Evtushenko T.P., Malyshev G.M., Ostrovskaya G.V., Semenov V.V., Chelidze T.Ya. *Zh. Tekh. Fiz.*, **36**, 1115 (1966).
19. Wilson J.R. *J. Phys. D: Appl. Phys.*, **3**, 2005 (1970).
20. Ignatov A.B., Komissarova I.I., Ostrovskaya G.V., Shapiro L.L. *Zh. Tekh. Fiz.*, **41**, 701 (1971).
21. Zhang Yi et al. *Chin. Phys.*, **16**, 3728 (2007).
22. Ostrovskaya G.V. *Zh. Tekh. Fiz.*, **78**, 1 (2008).
23. Soubacq S. et al. *J. Phys. D: Appl. Phys.*, **37**, 2686 (2004).
24. Morgan C.G. *Rep. Progr. Phys.*, **38**, 621 (1975).
25. Malyutin A.A. *Kvantovaya Elektron.*, **38**, 462 (2008) [*Quantum Electron.*, **38**, 462 (2008)].
26. Evans L.R., Morgan C.G. *Phys. Rev. Lett.*, **22**, 1099 (1969).
27. Vogel A., Nahen K., Theisen D., Birngruber R., Thomas R.J., Rockwell B.A. *Appl. Opt.*, **38**, 3636 (1999).
28. Ghosh S., Mahesh K. *J. Fluid Mech.*, **605**, 329 (2008).
29. Glumac N., Elliott G., Boguszko M. *AIAA J.*, **43**, 1984 (2005).
30. Zakharchenko S.V., Sintyurin G.A., Skripkin A.M. *Pis'ma Zh. Tekh. Fiz.*, **6**, 1065 (1980).
31. Malyutin A.A., Podvyaznikov V.A., Chevokin V.K. *Kvantovaya Elektron.*, **40**, 149 (2010) [*Quantum Electron.*, **40**, 149 (2010)].
32. Bagdasarov V.Kh., Denisov N.N., Malyutin A.A., Chigaev I.A. *Kvantovaya Elektron.*, **39**, 887 (2009) [*Quantum Electron.*, **39**, 887 (2009)].